

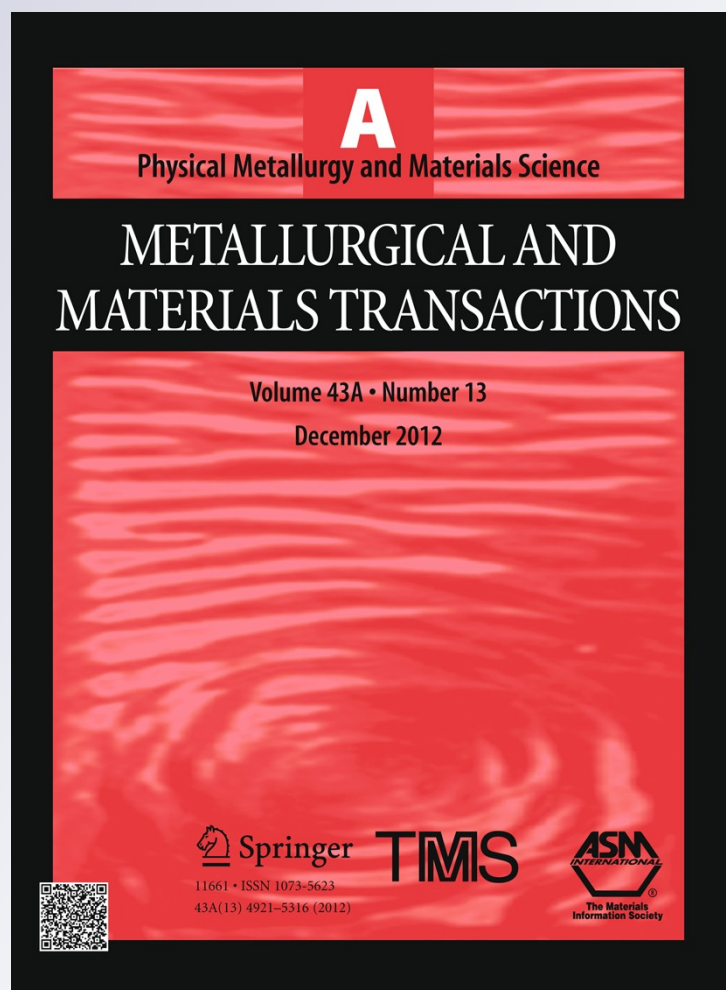
# *A Self-Consistent Approach for Necking Correction in Tensile Specimens With Rectangular Cross-Section Using a Novel Mirror Fixture*

**K. E. Yazzie, H. Fei, H. Jiang & N. Chawla**

**Metallurgical and Materials Transactions A**

ISSN 1073-5623  
Volume 43  
Number 13

Metall and Mat Trans A (2012)  
43:5058-5066  
DOI 10.1007/s11661-012-1355-6



**Your article is protected by copyright and all rights are held exclusively by The Minerals, Metals & Materials Society and ASM International. This e-offprint is for personal use only and shall not be self-archived in electronic repositories. If you wish to self-archive your work, please use the accepted author's version for posting to your own website or your institution's repository. You may further deposit the accepted author's version on a funder's repository at a funder's request, provided it is not made publicly available until 12 months after publication.**

# A Self-Consistent Approach for Necking Correction in Tensile Specimens With Rectangular Cross-Section Using a Novel Mirror Fixture

K.E. YAZZIE, H. FEI, H. JIANG, and N. CHAWLA

True stress–true strain cannot be computed beyond necking, unless the effects of necking on the geometry of the tensile specimen and the stress state are accurately quantified. Necking produces a triaxial stress state that does not reflect the true uniaxial flow stress of the material. Therefore, the true stress must be multiplied by a correction factor to correct for the effect of the triaxial stresses and obtain the true uniaxial flow stress. While necking effects are easily quantified for specimens with circular cross-sections, specimens with rectangular cross-sections can exhibit complex necking geometry. In this paper, the necking behavior of pure Sn and Sn-3.5Ag-0.7Cu solders was studied to: (1) quantify necking geometry in rectangular specimens using a novel mirror fixture and a high speed camera during tests conducted at  $10^{-3}$  to  $30 \text{ s}^{-1}$ , and (2) develop a self-consistent method of necking correction that incorporates strain rate effects and can be applied to many materials.

DOI: 10.1007/s11661-012-1355-6

© The Minerals, Metals & Materials Society and ASM International 2012

## I. INTRODUCTION

THE necking behavior, observed during tensile testing of metals, has been studied extensively.<sup>[1–12]</sup> Bridgman<sup>[1]</sup> analyzed the necking behavior for specimens with circular cross-section. In Bridgman's correction, the necking geometry is quantified using the curvature of the necked region,  $R$ , and the radius of the specimen,  $a$ . Then the equivalent true stress,  $\sigma_{\text{eq}}$ , is computed by multiplying the experimentally calculated axial stress,  $\sigma_{\text{ZZ}}$ , by a correction factor which is a function of the neck geometry:

$$\sigma_{\text{eq}} = \frac{\sigma_{\text{ZZ}}}{\left(1 + \frac{2R}{a}\right) \ln\left(1 + \frac{a}{2R}\right)} \quad [1]$$

The correction factor can be represented simply by  $\zeta$ ,

$$\sigma_{\text{eq}} = \sigma_{\text{ZZ}} \cdot \zeta \quad [2]$$

Where,

$$\zeta = \begin{cases} 1 & \text{prior to necking} \\ \frac{1}{\left(1 + \frac{2R}{a}\right) \ln\left(1 + \frac{a}{2R}\right)} & \text{after necking} \end{cases} \quad [3]$$

The Bridgman correction shows that correcting for necking requires a two-step process: First the neck geometry must be quantified, and then a correction factor can be calculated to obtain the equivalent true stress from the axial stress.

Though the Bridgman correction has been widely used, it can only be directly applied to samples with circular cross-section because it assumes an axisymmetric stress distribution.<sup>[1–3]</sup> Specimens with rectangular cross-section are frequently used due to ease of machining or limitations imposed by the starting material. However, efforts have been made to develop a necking correction for rectangular specimens. Aronofsky<sup>[4]</sup> showed that the stress distribution is not uniform in a necked rectangular specimen. Tvergaard<sup>[5]</sup> showed that the necking geometry is complex for rectangular tensile specimens and varies with aspect ratio. Some researchers have foregone the quantification of neck geometry by substituting  $a/R$  in Eq. [3] with the reduced strain,  $\varepsilon - \varepsilon_n$  where  $\varepsilon$  is the true plastic strain and  $\varepsilon_n$  is the true plastic strain at the onset of necking, multiplied by a constant.<sup>[6,7]</sup> While it has been shown that this method is within the error inherent to the Bridgman correction, it involves rigorous experimental work to determine the correct constant for each geometry and material.<sup>[8]</sup> Zhang *et al.*<sup>[9]</sup> developed an approximation to determine the necking geometry, but they relied on the Bridgman correction for determining true stress. Ling<sup>[10]</sup> developed a weighted average method to calculate equivalent true stress from the axial stress, but the weight constants in the formula are difficult to determine. Scheider *et al.*<sup>[11]</sup>

K.E. YAZZIE, formerly Graduate Research Associate, with Materials Science and Engineering, Arizona State University, Tempe, AZ 85287-6106, and is now Senior Engineer with Assembly Test and Technology Development, Intel Corporation, Chandler, AZ. H. FEI, formerly Graduate Research Associate, with Mechanical and Aerospace Engineering, Arizona State University, and is now Senior Engineer with Assembly Test and Technology Development, Intel Corporation. H. JIANG, Associate Professor, is with Mechanical and Aerospace Engineering, Arizona State University. N. CHAWLA, Fulton Professor of Materials Science and Engineering, is with Materials Science and Engineering, Arizona State University. Contact e-mail: nchawla@asu.edu

Manuscript submitted April 1, 2012.

Article published online August 7, 2012

developed a correction, but it is limited to flat, sheet-like geometries. Choung and Cho<sup>[12]</sup> developed a necking correction for rectangular specimens that was based on the strain hardening exponent,  $n$ , but a more general criterion needs to be developed that is independent of material. It is clear that a necking correction method, which accurately quantifies neck geometry and is self-consistent, is needed.

This paper presents work in which the necking behavior of Sn and Sn-3.5Ag-0.7Cu alloys were studied in order to create a self-consistent approach to calculate the degree of necking, and thus, the equivalent true stress, that can be applied to any material. The first part of the paper describes the experimental quantification of necking behavior, including the microstructure of the samples, and the use of a novel mirror fixture with a high speed camera to accurately quantify neck geometry in tensile specimens tested at  $10^{-3}$  to  $30 \text{ s}^{-1}$ . The second part of this paper discusses a self-consistent method of true stress correction. Self-consistency was obtained by iteratively comparing the measured experiment data and the numerical simulation results. The true stress corrections developed using the self-consistent method incorporate strain rate effects. Finally, the true stress–true strain behavior, obtained using the mirror fixture and strain rate-dependent necking corrections, is discussed.

## II. MATERIALS AND EXPERIMENTAL PROCEDURE

Sn-3.5Ag-0.7Cu (SAC) (Indium Corporation, Ithaca, NY) and 99.999 pct pure Sn (Alfa Aesar, Ward Hill, MA) ingots were melted in a graphite-coated aluminum mold by heating to  $20^\circ\text{C}$  above the melting point, holding for 20 seconds, and then cooling. A fine microstructure was produced in pure Sn by recrystallization after cold working 35 pct by rolling. The Sn had a final average grain size of about  $400 \mu\text{m}$ , as shown in Figure 1(a). Fine and coarse microstructures were obtained for SAC samples with a water quenched cooling rate of  $16.5^\circ\text{C/s}$  and a furnace cooling rate of  $1^\circ\text{C/s}$ , respectively. The water quenched SAC (WQ-SAC) microstructure consisted of Sn-rich dendrites and a eutectic mixture of Sn,  $\text{Cu}_6\text{Sn}_5$ , and  $\text{Ag}_3\text{Sn}$ , as shown in Figure 1(b). The furnace cooled SAC (FC-SAC) microstructure consisted of  $\text{Ag}_3\text{Sn}$  needles and  $\text{Cu}_6\text{Sn}_5$  intermetallic several micrometers in size, as shown in Figure 1(c). Rectangular tensile specimens were then machined from the ingots. Details about the specimen geometry are provided in Figure 1(d).

A mirror fixture was designed and machined from 304 stainless steel. Details about the design are available elsewhere.<sup>[14]</sup> The fixture was designed with first-surface

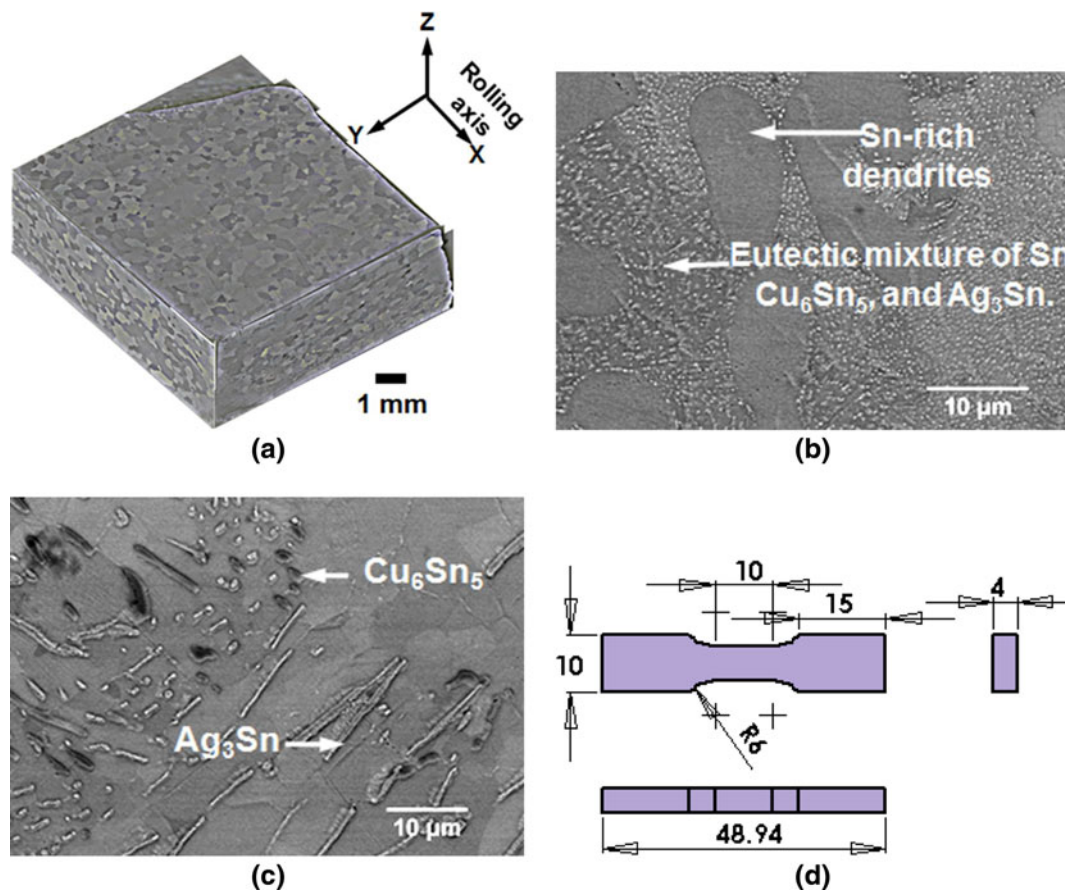


Fig. 1—(a) Microstructure of pure Sn. The average grain size was  $400 \mu\text{m}$ . (b) The microstructure of water quenched SAC. Sn-rich dendrites are surrounded by a eutectic mixture of  $\text{Cu}_6\text{Sn}_5$  and  $\text{Ag}_3\text{Sn}$  second phase precipitates. (c) The microstructure of furnace cooled SAC. Sn-rich regions are interspersed with  $\text{Cu}_6\text{Sn}_5$  and  $\text{Ag}_3\text{Sn}$  second phase precipitates. (d) The specimen geometry used in this study. All dimensions in mm.

mirrors attached, such that the instantaneous cross-sectional area of the specimen could be measured throughout the tensile tests. A first-surface mirror has the reflective surface above a backing, as opposed to a conventional mirror in which the reflective surface is behind a transparent medium such as glass. The mirror fixture was then gripped by a MTS 810 servohydraulic machine to complete the load train. Tensile tests were conducted in displacement control at nominal strain rates ranging from  $10^{-3} \text{ s}^{-1}$  to  $30 \text{ s}^{-1}$ . A high-speed camera (Phantom, Vision Research, Wayne, NJ) simultaneously recorded the right-angle reflections and front view of the tensile specimen at frame rates of up to 4,200 frames per second. High-intensity LED lights were stationed next to the mirror fixture to provide direct lighting without producing excess heat.

### III. RESULTS AND DISCUSSION

We begin by defining some simple stress-strain relations, before addressing the issue of necking. Engineering stress-strain was computed using Eq. [4].<sup>[15]</sup>

$$s = \frac{P}{A_0}, \quad e = \frac{\Delta L}{L_0} \quad [4]$$

where the axial load,  $P$ , is prescribed and the axial elongation,  $\Delta L$ , is recorded.  $A_0$  is the original cross-sectional area of the specimen and  $L_0$  is the original length. Before the onset of necking true stress-strain was obtained from engineering stress-strain via Eqs. [5] and [6].

$$\sigma = s(1 + e) \quad [5]$$

$$\varepsilon = \ln(1 + e) \quad [6]$$

After the onset of necking true stress-strain was computed using Eqs. [7] and [8].

$$\sigma = \frac{P}{A} \quad [7]$$

$$\varepsilon = \ln\left(\frac{A}{A_0}\right) \quad [8]$$

The minimum width,  $b$ , and minimum thicknesses,  $t_1$  and  $t_2$ , were manually measured in selected frames from the high speed video. Instantaneous minimum cross-sectional area was computed using the average of the two thicknesses:  $A = b[(t_1 + t_2)/2]$ . The experimentally determined true stress, which is not corrected for necking, is  $\sigma_{ZZ}^{\text{experiment}}$ , where the subscript  $zz$  refers to the axial direction.

$\sigma_{ZZ}^{\text{experiment}}$  was corrected for triaxial stresses, to give the equivalent true stress  $\sigma_{\text{eq}}$ , using the correction factor developed by Choung and Cho:

$$\zeta(\varepsilon_p) = \begin{cases} 1 & \text{for } \varepsilon_p < 1.4n \\ \alpha\varepsilon_p^2 + \beta\varepsilon_p + \gamma & \text{for } \varepsilon_p > 1.4n \end{cases} \quad [9]$$

where,  $\varepsilon_p$  is the plastic strain,  $\alpha = -0.0704n - 0.0275$ ,  $\beta = 0.4550n - 0.2926$ , and  $\gamma = 0.1592n + 1.024$ , and  $n$  is the strain hardening exponent, measured from the slope of  $\text{Log}\sigma\text{--Log}\varepsilon$ . The correction factor is only valid up to the onset of localized necking, after which rapid failure typically occurs. Therefore, equivalent true stress-true strain computed using Eq. [9] was only plotted up to the onset of localized necking, as identified from the high speed video.

#### A. Self-Consistent Method

The criterion of stress correction is specified as follows. The equivalent true stress is just the axial true stress prior to necking, or that obtained from the axial true stress multiplied by a correction function after the onset of necking. Then the equivalent true stress is used as input for a numerical model. The axial true stress computed from numerical analysis,  $\sigma_{ZZ}^{\text{numerical}}$ , is determined and will accurately reproduce the experimentally determined axial true stress if the input is correct. Figure 2 shows a flow chart that describes the self-consistent method. The method starts with the experimentally determined axial true stress, which is then corrected using a trial correction function,  $\zeta$ , to give the equivalent true stress,  $\sigma_{\text{eq}}$ . Using the equivalent true stress, a finite element analysis is conducted and the axial true stress is calculated. Then, a new correction function,  $\zeta^{\text{new}}$ , is obtained based on the axial true stress from numerical modeling, and the corrected equivalent true stress. Then the axial true stresses determined from experiment,  $\sigma_{ZZ}^{\text{experiment}}$ , and from numerical analysis,  $\sigma_{ZZ}^{\text{numerical}}$ , is compared via the least squares method. If the correction function is not accurate, it is updated to  $\zeta^{\text{new}}$  and the self-consistent method will be reiterated until  $\sigma_{ZZ}^{\text{experiment}} = \sigma_{ZZ}^{\text{numerical}}$ . Finally, the correction function  $\zeta$  is fitted as a function of true strain and strain rate to formulate the necking correction function.

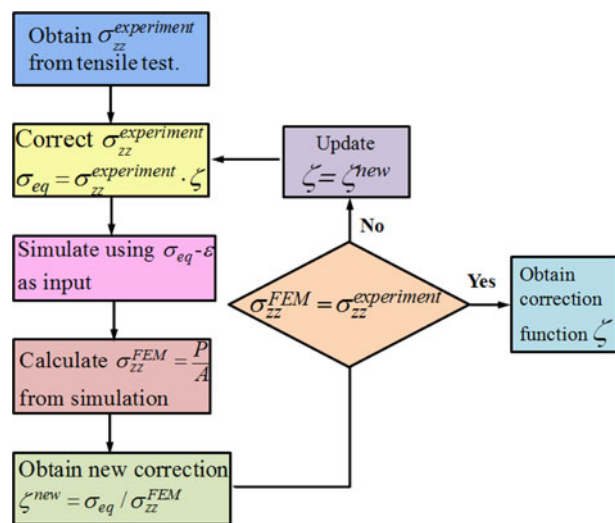


Fig. 2—Flow chart of self-consistent method for necking correction. This method can be applied to many materials.

The self-consistent method was applied using equivalent true stress, computed from experimental tensile tests and Eq. [9], as the material input for a finite element method (FEM) simulation executed using commercial FEM package ABAQUS. Figure 3 shows the symmetric geometry used for the simulation. The geometry is a quarter of the real specimen, and symmetric boundary conditions are applied on the two symmetric surfaces. Eight-node brick elements (C3D8) are used for discretization. Mesh sensitivity has been studied, and a typical finite element mesh with 25,000 elements that leads to converged results is shown in Figure 3. A velocity load was applied to the end of the specimen, to produce strain rates equal to the experimentally applied strain rates. True stress was measured in a manner consistent with experiment. The force in the tensile direction was measured from reaction forces at the end of the model at each time increment. The minimum instantaneous cross-section area was also measured at each time increment.  $\sigma_{zz}^{\text{numerical}}$  was obtained from simulation using Eq. [7], while the true strain in the

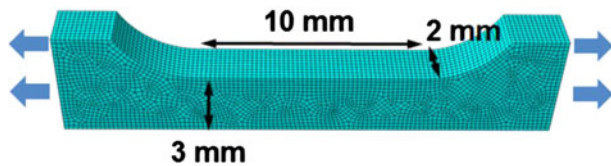


Fig. 3—The FEM model used for computing the necking correction.  $\frac{1}{4}$  of the experimental specimen geometry was modeled with symmetric boundary conditions applied. There were 25,000 eight-node brick elements (C3D8) in the system.

tensile direction was measured from the average true plastic strain of all the elements.

### B. Necking Correction

The experimentally measured stress–strain curve for Sn tested at  $10 \text{ s}^{-1}$  is used as an example to show the accuracy of using the mirror fixture and the self-consistent method to quantify and correct for necking.

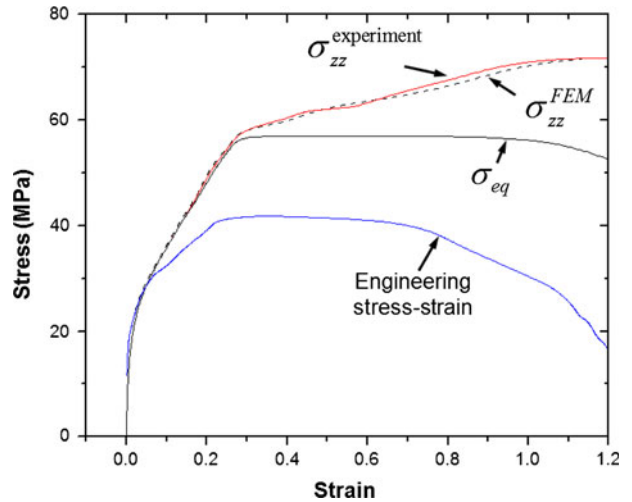


Fig. 5—Stress–strain curves for Sn tested at  $10 \text{ s}^{-1}$ . The curves indicate that using the correction function  $\zeta = -0.048\epsilon^2 - 0.161\epsilon + 1.07$  yields an axial stress measured from the simulation that is consistent with the experimentally determined axial stress, thereby validating this correction function.

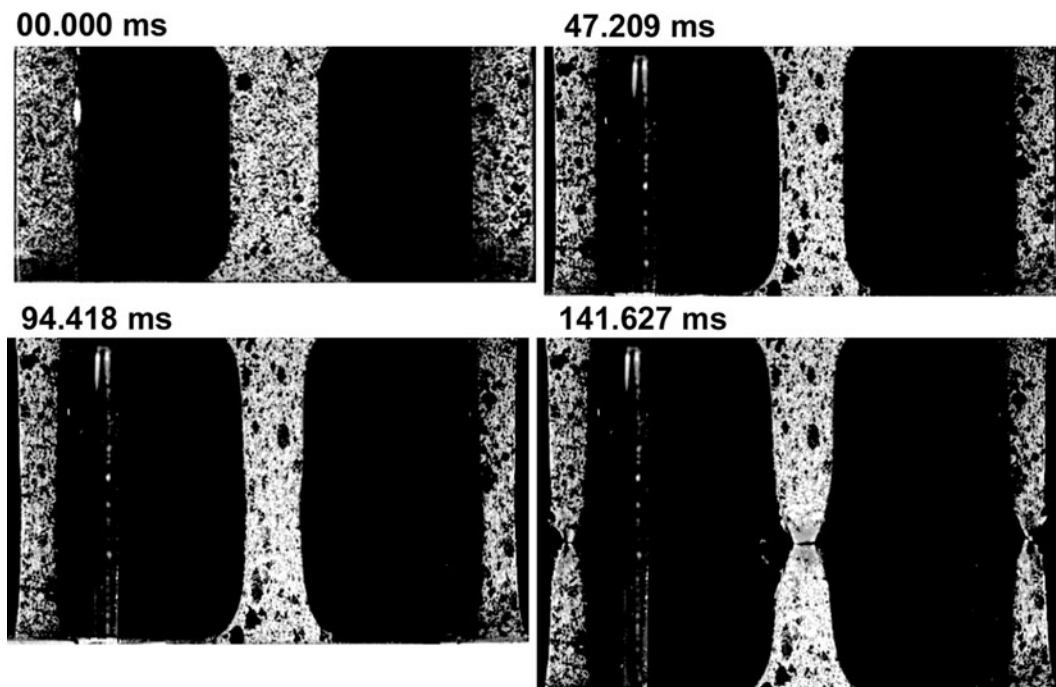


Fig. 4—Tensile test of recrystallized pure Sn tested at  $10 \text{ s}^{-1}$  using mirror fixtures. The mirror fixture produced right-angle reflections of the left and right sides of the tensile specimen while the high speed camera recorded the deformation of all three sides, including the front face. Time elapsed from the start of the test is indicated at the bottom of the images in milliseconds.

Images of the test are shown in Figure 4. It can be seen that the mirror fixture and high speed camera produced high quality images that allowed for the instantaneous minimum width and thickness to be measured throughout the test. The stress-strain curves for this test, shown in Figure 5, indicate that using the correction function,

$$\zeta = -0.048\varepsilon^2 - 0.161\varepsilon + 1.07 \quad [10]$$

yields an axial stress measured from the simulation,  $\sigma_{zz}^{\text{numerical}}$ , that is consistent with the experimentally determined axial stress  $\sigma_{zz}^{\text{experiment}}$ . Note that this correction function is quite different from that obtained by applying Choung and Cho's method.<sup>[12]</sup> It will now be shown how a general correction function can be found for each material.

The general necking correction function, excluding strain rate dependence, is represented by a function of the form:

$$\zeta_{\text{material}}(\varepsilon) = a\varepsilon + b \quad [11]$$

Where the subscript refers to the material and its microstructural state, (e.g., Sn, WQ-SAC, FC-SAC) and  $a$  and  $b$  are constants. This function was obtained by computing a least-squares linear fit to all the necking correction data points calculated for individual tests, irrespective of the applied strain rate. Figure 6 shows the necking correction data points for individual tests for: (a) Sn, (b) WQ-SAC, and (c) FC-SAC. The linear fit which gave the general necking correction function is shown in Figure 7 for (a) Sn, (b) WQ-SAC, and (c) FC-SAC. The necking correction functions are:

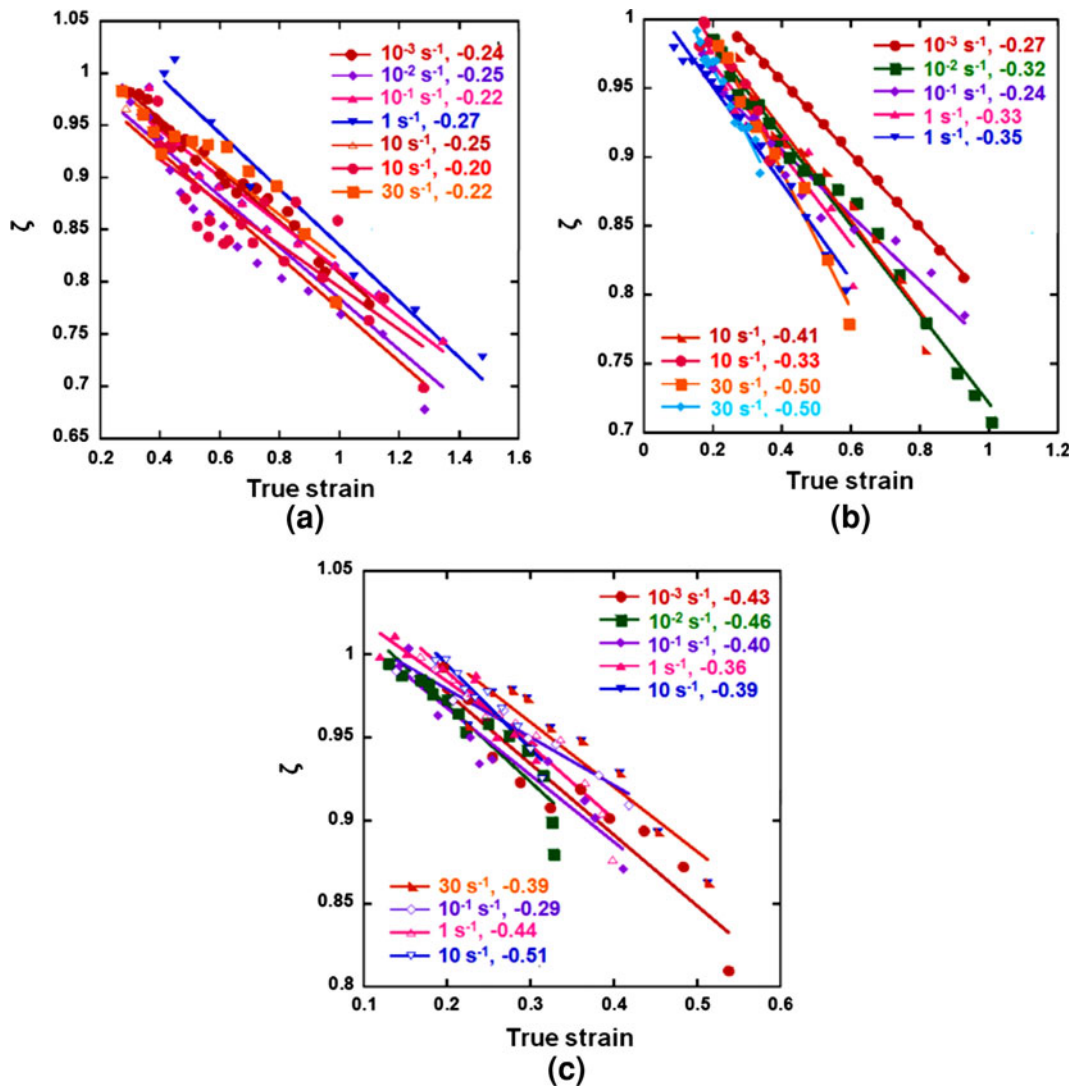


Fig. 6—(a) Data points of necking correction functions computed for each test and plotted as a function of true strain for Sn. A least-squares linear fit was calculated for each test. The slope of the linear fit is indicated in the inset legends. (b) Data points of necking correction functions, computed for each test and plotted as a function of true strain for water quenched SAC. A least-squares linear fit was calculated for each test. The slope of the linear fit is indicated in the inset legends. (c) Data points of necking correction functions computed for each test and plotted as a function of true strain for furnace cooled SAC. A least-squares linear fit was calculated for each test. The slope of the linear fit is indicated in the inset legends.

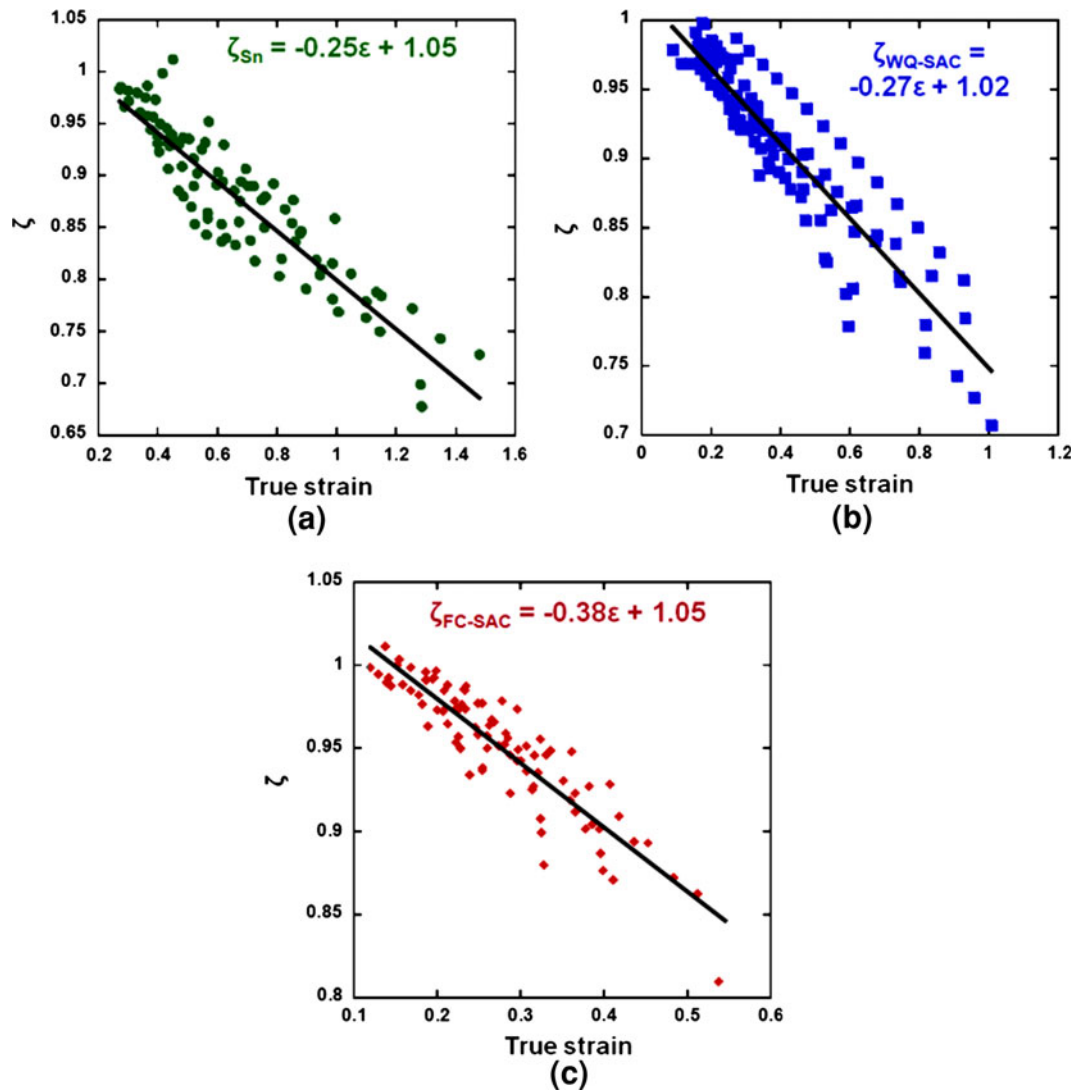


Fig. 7—(a) Data points of necking correction functions for all tests plotted irrespective of the applied strain rate and as a function of true strain for Sn. Least-squares linear fits gave the necking correction function for this material without strain rate dependence. The necking correction function is indicated. (b) Data points of necking correction functions for all tests plotted irrespective of the applied strain rate and as a function of true strain for water quenched SAC. Least-squares linear fits gave the necking correction function for this material without strain rate dependence. The necking correction function is indicated. (c) Data points of necking correction functions for all tests plotted irrespective of the applied strain rate and as a function of true strain for furnace cooled SAC. Least-squares linear fits gave the necking correction function for this material without strain rate dependence. The necking correction function is indicated.

$$\zeta_{\text{Sn}}(\varepsilon) = -0.25\varepsilon + 1.05 \quad [12]$$

$$\zeta_{\text{WQ-SAC}}(\varepsilon) = -0.27\varepsilon + 1.02 \quad [13]$$

$$\zeta_{\text{FC-SAC}}(\varepsilon) = -0.38\varepsilon + 1.05 \quad [14]$$

While several methods for correcting true stress for necking effects have been developed,<sup>[1,8–12]</sup> none have explicitly incorporated strain rate-dependent material behavior. This is an important consideration, since many materials exhibit strain rate-dependent mechanical behavior.<sup>[15]</sup> Indeed, the materials characterized in this study, Sn and Sn-rich alloy, are known to be significantly strain rate sensitive.<sup>[16,17]</sup> Therefore,

in the following section the strain rate dependent necking corrections were computed for each material.

The strain rate-dependence of the necking correction function is represented by the slope of the necking correction data points for individual tests. Specifically, the change in the slope with the applied strain rate quantifies the strain rate dependence. Least-squares linear fits were computed for the individual tests, as shown in Figure 6, with the slopes indicated in inset legends. The slopes were plotted as function of Log of the applied strain rate in Figure 8. Strain rate dependence was incorporated into Eq. [13] by substituting  $a$  with a least-squares linear fit computed for the data points shown in Figure 8. The strain rate dependent necking correction function is then

$$\zeta_{\text{material}}(\varepsilon, \dot{\varepsilon}) = (c \text{Log} \dot{\varepsilon} + d)\varepsilon + b \quad [15]$$

$$\zeta_{\text{FC-SAC}}(\varepsilon, \dot{\varepsilon}) = (-0.019 \cdot \text{Log} \dot{\varepsilon} - 0.440) \cdot \varepsilon + 1.05 \quad [18]$$

where  $c$  and  $d$  are constants. The strain rate-dependent necking corrections for Sn, WQ-SAC, and FC-SAC are given below.

$$\zeta_{\text{Sn}}(\varepsilon, \dot{\varepsilon}) = (0.004 \cdot \text{Log} \dot{\varepsilon} - 0.235) \cdot \varepsilon + 1.05 \quad [16]$$

$$\zeta_{\text{WQ-SAC}}(\varepsilon, \dot{\varepsilon}) = (-0.045 \cdot \text{Log} \dot{\varepsilon} - 0.366) \cdot \varepsilon + 1.02 \quad [17]$$

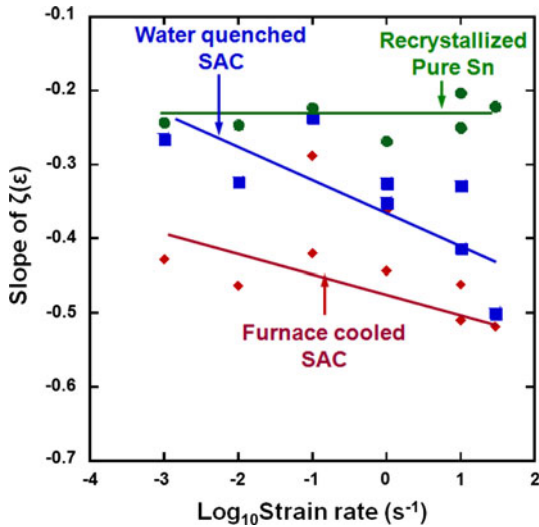


Fig. 8—Slopes of the linear fits computed for the necking correction data points in Fig. 6 were plotted as a function of the applied strain rate for Sn, water quenched SAC, and furnace cooled SAC. The data points were approximated by least-squares linear fits. The linear fits quantify the strain rate dependence of the necking correction function.

The strain rate dependence of the Sn necking correction is an order of magnitude weaker than that for water quenched and furnace cooled SAC. This is not surprising, since Sn is very ductile, even at strain rates up to  $30 \text{ s}^{-1}$ ,<sup>[13]</sup> and necks quite uniformly. The strain rate dependence of the Sn necking correction is therefore, negligible. Furnace cooled SAC necking correction has a stronger strain rate dependence, due to the strain hardening produced by the second phase precipitates of  $\text{Ag}_3\text{Sn}$  and  $\text{Cu}_6\text{Sn}_5$ .<sup>[18]</sup> However, these precipitates are quite large. Water quenched SAC necking correction has the strongest strain rate dependence, due to the greater strain hardening produced by the fine dispersion of spherical  $\text{Ag}_3\text{Sn}$  precipitates.<sup>[18]</sup> These precipitates serve as more effective barriers to dislocation motion, compared to the large precipitates in furnace cooled SAC.<sup>[18,19]</sup> In the next section, the strain rate-dependent necking correction factors will be applied to experimentally measured true stress–true strain curves.

### C. Equivalent True Stress–True Strain Curves for Sn and Sn-3.5Ag-0.7Cu

In order to qualitatively show how effective the strain rate-dependent necking correction factors are at correcting for triaxial stresses, stress–strain curves for Sn tested at (a)  $10^{-3} \text{ s}^{-1}$  and (b)  $30 \text{ s}^{-1}$  were compared in Figure 9. Equivalent true stress–true strain curve was computed using Eq. [16]. As expected the true stress–true strain curve shows stresses and strains that are higher than their engineering stress–engineering strain counterparts. Also shown are equivalent true stress–true

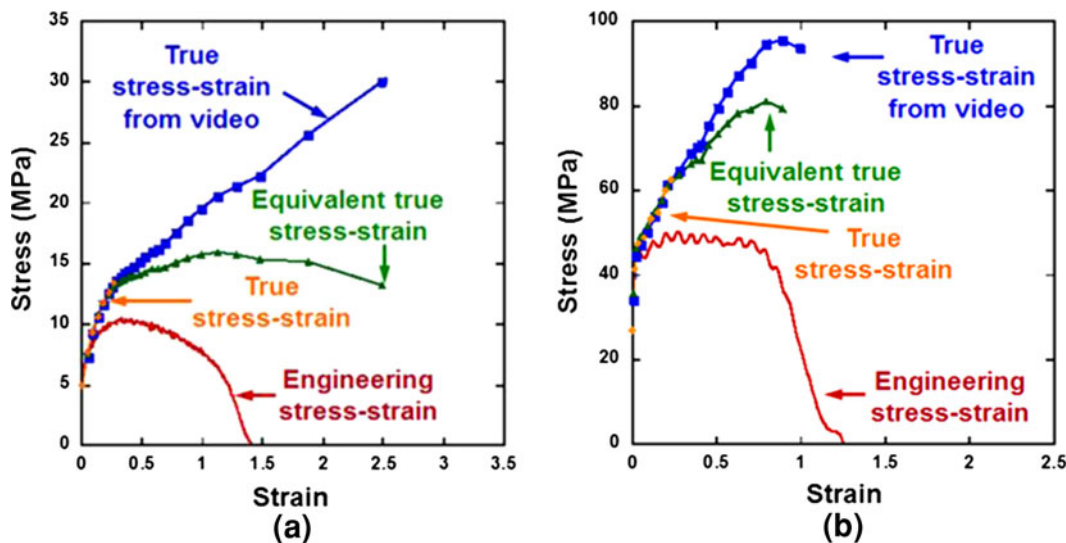


Fig. 9—(a) Engineering stress–strain curve, true stress–strain computed up to necking, true stress–strain computed beyond necking using the mirror fixtures, and the corrected true stress–strain for Sn tested at  $10^{-3} \text{ s}^{-1}$ . These examples show that there is a significant difference in flow stress for constitutive behavior that does not accurately quantify necking. (b) Engineering stress–strain curve, true stress–strain computed up to necking, true stress–strain computed beyond necking using the mirror fixtures, and the corrected true stress–strain are shown for Sn tested at  $30 \text{ s}^{-1}$ . These examples show that there is a significant difference in flow stress for constitutive behavior that does not accurately quantify necking.

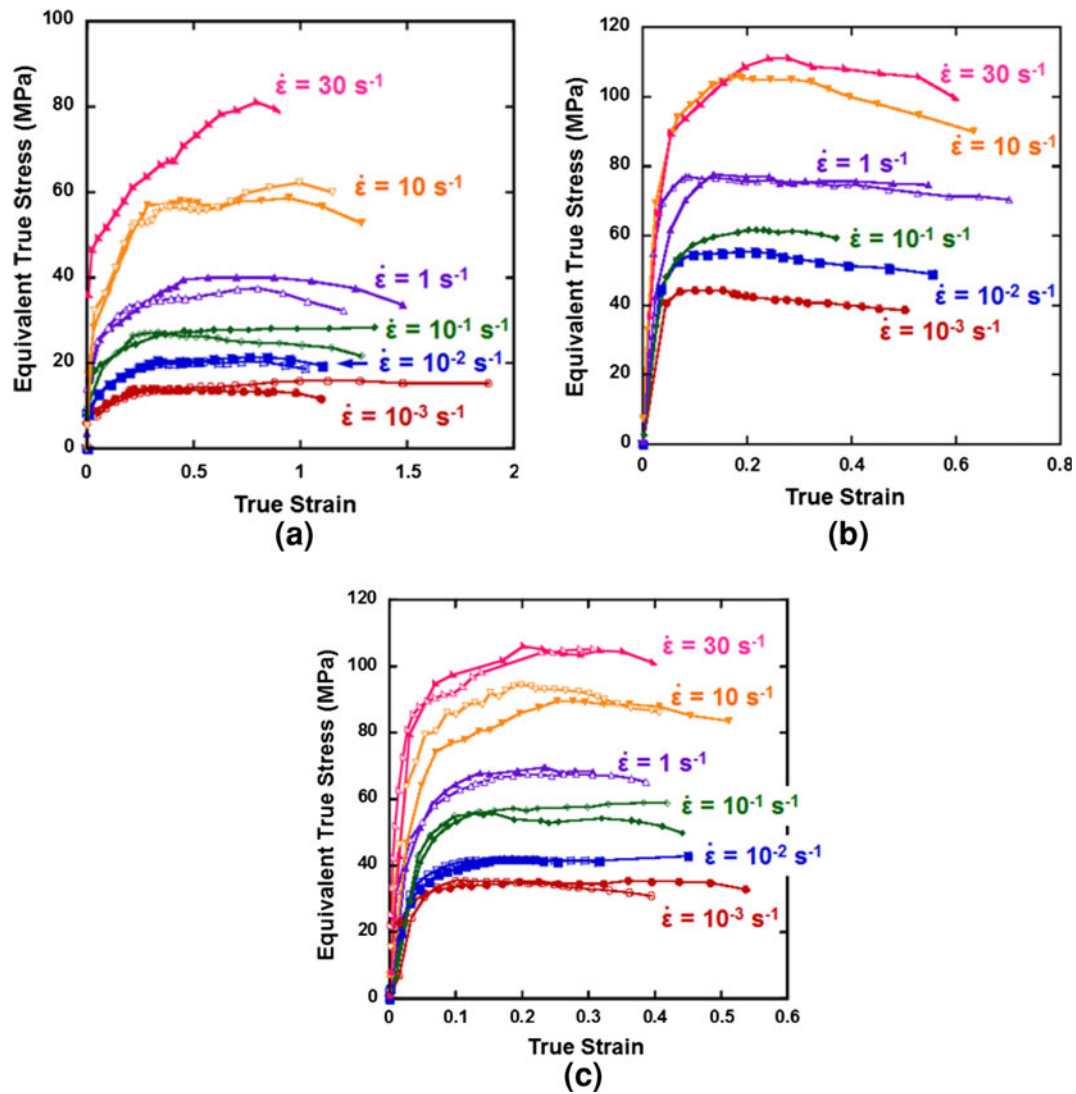


Fig. 10—(a) Equivalent true stress–true strain curves for Sn computed using Eq. [16]. Flow stress increases with the applied strain rate. The strain hardening rate also appears to increase with strain rate. (b) Equivalent true stress–true strain curves for water quenched SAC computed using Eq. [17]. Flow stress increases with the applied strain rate. The strain hardening rate also appears to increase with strain rate. (c) Equivalent true stress–true strain curves for furnace cooled SAC computed using Eq. [18]. Flow stress increases with the applied strain rate. The strain hardening rate also appears to increase with strain rate. When available, duplicate tests have been indicated with hollow symbols.

strain curves which have been corrected for triaxial stresses. Engineering stress–engineering strain underestimates the flow stress because necking geometry is not accurately represented by the original cross-sectional area. While true stress–true strain computed using the video accurately quantifies the necking geometry, it overestimates the flow stress because it has not been corrected for the triaxial stresses produced by necking. Therefore, equivalent true stress–true strain corrected using Eq. [16] accurately reflects the true flow behavior.

Figure 10 shows the equivalent true stress–true strain curves for (a) Sn, (b) water quenched SAC, and (c) furnace cooled SAC. Duplicate tests are shown when possible, and are represented by hollow symbols. In general, all tests showed an increase in flow stress with increasing strain rate. Pure Sn had the lowest flow stress for a given strain rate. Furnace cooled SAC had higher flow stresses than pure Sn, due to strengthening from

large  $\text{Ag}_3\text{Sn}$  needles and  $\text{Cu}_6\text{Sn}_5$  particles. Water quenched SAC had the largest flow stresses for a given strain rate, due to a finer microstructure, particularly in the form of a fine dispersion of  $\text{Ag}_3\text{Sn}$  and  $\text{Cu}_6\text{Sn}_5$  particles, that increased the number of obstacles for dislocation motion. Wong *et al.*<sup>[16]</sup> computed true stress–true strain curves for an alloy of similar composition, Sn-3.0Ag-0.5Cu, over the range of strain rates,  $0.1 \text{ s}^{-1}$ – $300 \text{ s}^{-1}$ . They observed a similar increase in flow stress with strain rate, and concluded that Sn-rich alloys are significantly strain rate sensitive. Siviour *et al.*<sup>[20]</sup> computed true stress–true strain curves for Sn-3.8Ag-0.7Cu alloy tested over a higher strain rate range of  $430 \text{ s}^{-1}$  to  $3,600 \text{ s}^{-1}$ . Conversely to Wong *et al.*,<sup>[16]</sup> they concluded that Sn-3.8Ag-0.7Cu exhibited little strain rate sensitivity over this range of strain rates. Indeed, in their study the true flow stress only increased from  $\sim 200 \text{ MPa}$  to  $\sim 220 \text{ MPa}$  when the strain rate was

increased from  $430 \text{ s}^{-1}$  to  $2800 \text{ s}^{-1}$ . This discrepancy may be explained by the fact that Wong *et al.*<sup>[16]</sup> and Siviour *et al.*<sup>[20]</sup> conducted tests in two different strain rate regimes which may be associated with different deformation mechanisms. Indeed, Long *et al.*<sup>[19]</sup> hypothesized that the low strain rate mechanical behavior of Sn-3.8Ag-0.7Cu may be controlled by dislocation particle-bypass mechanisms, while at high strain rates the dominant deformation mechanism is twinning in Sn-rich phases. Recently, Peirs *et al.*<sup>[21]</sup> utilized digital image correlation (DIC), a technique for measuring full-field strain on sample surfaces, to measure local strain during high strain rate tensile tests. They used the local strain values to estimate true stress–true strain and to validate FEM models of the high strain rate tensile test. Local DIC measurements, such as those made by Peirs *et al.*, may be able to characterize the strain rate-dependence of deformation mechanisms in Sn-rich alloys. And combined with the self-consistent method developed in this study, it may be possible to develop necking correction functions which accurately capture the complex deformation behavior of Sn-rich alloys over several different strain rate regimes.

#### IV. CONCLUSIONS

In order to reliably measure constitutive behavior of materials from tensile tests of rectangular specimens, the effect of necking on the geometry of the specimen and the stress state must be accurately quantified. The following conclusions are made, based on the experimental results.

1. Necking in rectangular specimens can produce a complicated cross-sectional geometry. Therefore a way of measuring both width and thickness on multiple specimen faces was needed. To be compatible with testing over multiple strain rates, the measurement system needed to be non-contact. The novel mirror fixture solves both these problems, and can be used for with other materials.
2. True stress–true strain computed using the instantaneous minimum cross-sectional area measured with the mirror fixture corrects the engineering stress–engineering strain for the effect of the neck geometry. However, this does not correct for the effect of triaxial stresses produced by the neck geometry. A correction function must be applied to the true stress to correct for the triaxial stresses.
3. A self-consistent method was used to develop necking correction functions. The method results in the expected trends in axial true stress. The self-consistent nature of the method means that its accuracy is not limited to a specific material. The method may be applied to all materials, once the axial true stress is calculated from tensile tests.
4. The necking corrections developed for Sn and Sn-3.5Ag-0.7Cu solders incorporated strain rate effects. The Sn necking correction had the least strain rate dependence, while the furnace cooled SAC necking correction had moderate strain rate dependence,

and the water quenched SAC necking correction had the strongest strain rate dependence. This was explained by the strain hardening produced by second phase precipitates of  $\text{Ag}_3\text{Sn}$  and  $\text{Cu}_6\text{Sn}_5$ , which Sn lacks. The precipitates were large in furnace cooled SAC and did not pose significant obstacles to dislocation motion. The precipitates in water quenched SAC were small and numerous, and served as excellent barriers to dislocation motion.

#### ACKNOWLEDGMENTS

The authors are grateful for the financial support for this work from the National Science Foundation Division of Materials Research—Metals Division (Drs. Alan Ardell, Bruce MacDonald, and Harsh Chopra, Program Directors). The authors gratefully acknowledge the use of facilities within the Center for Solid State Science at Arizona State University.

#### REFERENCES

1. P.W. Bridgman: *Studies in Large Plastic Flow and Fracture: With Special Emphasis on the Effects of Hydrostatic Pressure*, Harvard University Press, Cambridge, 1964.
2. M. Alves and N.J. Jones: *Mech. Phys. Solids*, 1999, vol. 47, pp. 643–67.
3. J.C. Earl and D.K. Brown: *Eng. Fract. Mech.*, 1976, vol. 8, pp. 599–602.
4. J. Aronofsky: *J. Appl. Mech.*, 1951, vol. 18, pp. 75–84.
5. V. Tvergaard: *Comput. Meth. Appl. Mech. Eng.*, 1993, vol. 103, pp. 273–90.
6. G. Le Roy, J.D. Embury, G. Edwards, and M.F. Ashby: *Acta Metall.*, 1981, vol. 29, pp. 1509–22.
7. A.R. Ragab: *Int. J. Fract.*, 2000, vol. 105, pp. 391–409.
8. G. Rosa, A. Risitano, and G. Mirone: *Metall. Mater. Trans. A*, 2003, vol. 34A, pp. 615–24.
9. Z.L. Zhang, M. Hauge, J. Odegaard, and C. Thaulow: *Int. J. Solids Struct.*, 1999, vol. 36, pp. 3497–3516.
10. Y. Ling: *AMP J. Technol.*, 1996, vol. 5, pp. 37–48.
11. I. Scheider, W. Brocks, and A. Cornec: *J. Eng. Mater. Technol.*, 2004, vol. 126, pp. 70–76.
12. J.M. Choung and S.R. Cho: *J. Mech. Sci. Technol.*, 2008, vol. 22, pp. 1039–51.
13. K.E. Yazzie, H. Fei, J.J. Williams, H. Jiang, and N. Chawla: *J. Electron. Mater.*, 2009, vol. 38, pp. 2746–55.
14. K.E. Yazzie, J.J. Williams, and N. Chawla: *Mater. Lett.*, 2012, vol. 74, pp. 243–46.
15. M.A. Meyers and K.K. Chawla: *Mechanical Behavior of Materials*, Cambridge University Press, Cambridge, 2009.
16. E.H. Wong, C.S. Selvanayagam, S.K.W. Seah, W.D. van Driel, J.F.J.M. Caers, X.J. Zhao, N. Owens, L.C. Tan, D.R. Frear, M. Leoni, Y.S. Lai, and C.L. Yeh: *Mater. Lett.*, 2008, vol. 62, pp. 3031–34.
17. K.E. Yazzie, H.X. Xie, J.J. Williams, and N. Chawla: *Scripta Mater.*, 2012, vol. 66, pp. 586–89.
18. K.E. Yazzie, J.J. Williams, D. Kingsbury, P. Peralta, H. Jiang, and N. Chawla: *JOM*, 2010, vol. 62, pp. 16–21.
19. X. Long, I. Dutta, V. Sarihan, and D.R. Frear: *JEM*, 2008, vol. 37, pp. 189–200.
20. C.R. Siviour, S.M. Walley, W.G. Proud, and J.E. Field: *J. Phys. D: Appl. Phys.*, 2005, vol. 38, pp. 4131–39.
21. J. Peirs, P. Verleysen, W. Van Paepegem, and J. Degrieck: *Int. J. Impact Eng.*, 2011, vol. 38, pp. 406–15.